

Observations of internal waves and associated mixing phenomena in the Portimao Canyon area

M. Bruno^{a,*}, A. Vázquez^a, J. Gómez-Enri^a, J.M. Vargas^b, J. García Lafuente^b,
A. Ruiz-Cañavate^a, L. Mariscal^a, J. Vidal^a

^a*Departamento de Física Aplicada, Universidad de Cádiz, Av/ República Saharaui s/n, 11510-Puerto Real, Cádiz, Spain*

^b*Departamento de Física Aplicada II, Universidad de Málaga, Campus de Teatinos, 29071, Málaga, Spain*

Received 1 June 2005; accepted 2 April 2006

Abstract

Internal wave activity and induced mixing phenomena in the Portimao Canyon area (southern Portuguese coast) are analysed. Observations of current velocities and CTD measurements were taken during a 24-h period at two fixed stations located along the main axis of the canyon. The station nearest shore was located close to the canyon head and the other station was 5 km seaward. These basic measurements are complemented with vertical sections of temperature, acquired by XBT casts, along the main axis of the canyon, and also with time series of temperatures recorded by a thermistor chain moored on the continental shelf, near the canyon head. The time sequences of velocities and density profiles recorded at the fixed stations were analysed using a procedure based on empirical orthogonal function (EOF) analysis and dynamical modes decomposition (DMD) techniques. By this method, two different sources for internal wave activity are identified: a clear internal tide signal on the one hand, and a shorter than tidal period internal waves which exhibit greater current velocities and density oscillation amplitudes than internal tide, on the other. It is suggested that these shorter period internal waves are responsible for the vertical mixing affecting the water column over the slope and shelf waters in this region. Finally, it is also suggested that the evacuation of these mixed water masses formed around the continental shelf break may be related to a core of relatively cold water flowing over the continental slope toward west.

© 2006 Elsevier Ltd. All rights reserved.

Keywords: Gulf of Cádiz; Portimao submarine canyon; Internal tide; Short period internal waves

1. Introduction

Since the early works of Sandstrom (1966) and Wunsch (1968), internal waves generated at the shelf break have been identified as one of the more active mechanisms producing mixing between slope and

shelf waters. The most studied case is that related to the internal tide, which leads to the creation of the so-called tidal fronts over the continental shelf. Superimposed on the internal tide, other shorter period internal waves may take place, giving a noticeable contribution to mixing. These shorter period waves are usually a phenomenon inherent to the internal tide dynamic, arising from the desintegration of previously formed internal bores as a consequence of nonlinear effects imposed on the

*Corresponding author. Tel.: +34 9560 16076;
fax: +34 9560 16079.

E-mail address: Miguel.Bruno@uca.es (M. Bruno).

internal tide during its propagation (see Vlasenko and Alpers, 2005, for instance). In continental slopes where submarine canyons exist, internal wave generation may be favoured due to the increased intensity of currents through the canyon (Petrunco et al., 1998; García Lafuente et al., 1999). From the available analytical and numerical models, it is known that internal wave generation at the bottom of the continental slope may propagate its energy from the bottom of the slope waters to near or even over the shelf when the parameter

$$\beta = \frac{c}{h_x},$$

where c is the slope of the characteristic lines (lines on which the internal wave energy travels) and h_x is the bottom slope, is less than or equal to 1, (critical or subcritical, respectively). On the other hand, when β is greater than 1, the bottom slope is supercritical and the internal wave energy is reflected toward the ocean, preventing the associated internal wave mixing phenomena in the shelf waters from taking place.

The western coastal area of the Gulf of Cádiz seems to be a region favourable for the creation of vertical mixing and thermal fronts associated with internal wave dynamics. This expectation is sup-

ported by the examination of the bottom topography across the slope and shelf waters. From this analysis, the values of parameter β close to the shelf break show that bottom slopes there are nearly critical, and therefore internal tides may be efficiently generated and propagated in both shoreward and seaward directions.

In this work, observations of internal waves activity in the Portimao Canyon located along the southern Portuguese coast will be shown. Furthermore, the role of these phenomena in the exchange of properties between the slope and shelf waters will be analysed.

2. Field experiment

The field experiment was carried out as part of Oceanographic survey “GOLFO 2001” onboard the R.V. *Hespérides* 24–29 June 2001. It was designed to record and characterise the internal tide signature and other shorter-period internal waves generated in the Portimao canyon and the associated mixing processes. The location of the area under study, the grid of stations and the transects along which the axis of the canyon was sampled are shown on the map in Fig. 1. The field experiment consisted of three phases.

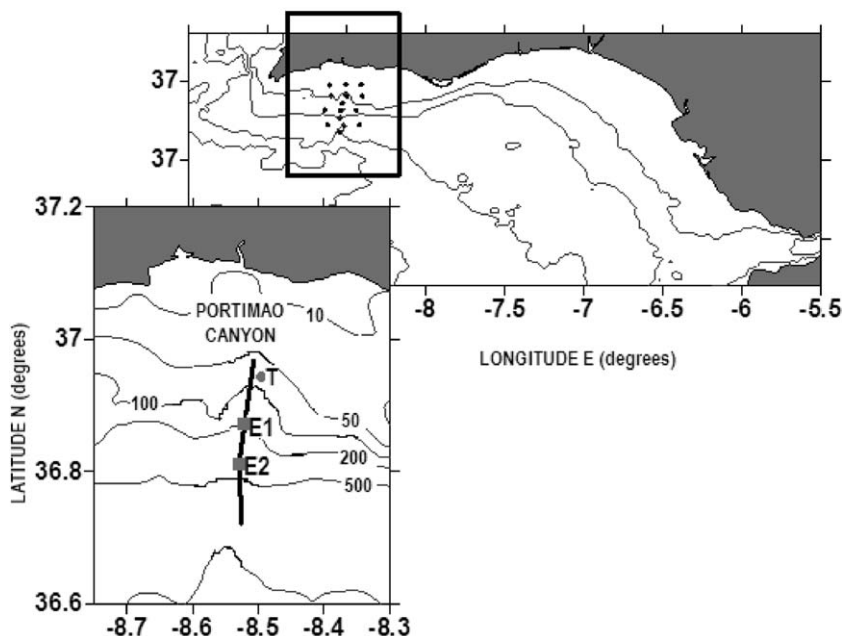


Fig. 1. Map of the studied region indicating the measurement locations. The upper panel shows the grid stations to record synoptic features around de Portimao Canyon. Points ‘E1’ and ‘E2’ in the lower panel, are fixed stations where ADCP and CTD observations during 24 h were recorded. Solid line is the ship track along which temperature profiles from XBT casts and ADCP measurements were taken. ‘T’ indicates the position where a chain with 5 thermistors was moored.

Phase 1. Sampling of a local network of CTD stations and ADCP transects to get a synoptic view of the mass and velocity fields in the area around the Portimao Canyon. These observations have been used to obtain representative profiles of density and buoyancy frequency necessary to construct the analytical framework in which internal wave observations will be interpreted.

Phase 2. Repetitive CTD sampling at two stations located at the mouth and at the head of the canyon (Fig. 1), spanning a 24-h period, to record internal tide signals. ADCP measurements were acquired continuously at a sampling interval of 1 min. The time interval between each pair of measurements at the stations was about 4 h. This relatively large time interval was occasioned by the collection of water samples at several depths in order to analyse some bio-chemical variables.

Phase 3. Rapid XBT casts along the canyon axis in order to record spatial structures associated with internal waves.

In addition to these observations, we have used time series of temperature acquired by a thermistor chain moored at the head of the Portimao Canyon (see Fig. 1), during a survey onboard R.V. “*Tofuño*” carried out in November 2001. The location of the mooring is indicated in Fig. 1.

3. Analysis of internal wave observations

The analysis presented here uses the CTD time series taken at the head of the Portimao Canyon during phase 2, and the ADCP time series taken at the head of the canyon and at another location seaward of it. The spatial analysis of the internal wave is based on the data taken during phase 3 of the field experiment. The analysis procedure involves two techniques: (i) The empirical orthogonal function decomposition, and (ii) the dynamical modes decomposition. A brief description of the role of each in the analysis procedure follows.

3.1. Empirical orthogonal functions decomposition

Empirical orthogonal functions (EOF) is a technique widely used in physical oceanography since the early work of Kundu et al. (1975). It is one of the techniques that allows the decomposition of the spatial and temporal variations of a given variable, recorded at several locations, into spatial distribution patterns, grouping signals that present common (or coherent) behaviour in their variations

with time. Once these common patterns are determined, the signal of the analysed variables may be expressed as

$$s(z, t) = \sum_{j=1}^M e_j(z) a_j(t), \quad (1)$$

where z denote spatial position (i.e. vertical coordinate), t is time, $e_j(z)$ are the EOFs, $a_j(t)$ are the temporal amplitudes of the EOFs and M is the number of EOFs (equal to the number of time series included into analysis).

When EOF is applied to the analysis of vertical structure of a current velocity time series, it is generally agreed that one of the empirical functions is associated with the barotropic part of the current oscillations. Based on this, EOF has been presented as a useful technique to separate barotropic and baroclinic variability in the time variations of currents (i.e. tidal currents) (Candela et al., 1990; Bruno et al., 2000; García Lafuente et al., 2000).

However, Bruno et al. (2000) reports that when the temporal variations of barotropic and baroclinic signals are nearly in phase or anti-phase, these modes are no longer separated. In this work, EOF is not used to separate barotropic and baroclinic signals in the current velocity records, but to separate signals with different time scales. This ability of EOF analysis is important in the analysed region where several sources of time variability are active. Satellite images observations show that the southern Portuguese coast is frequently occupied by density fronts along the coast (Folkard et al., 1997). It was also the case during our field experiment (see Fig. 5A of García Lafuente et al., 2006). Density fronts may develop baroclinic instabilities (Kundu, 1990; Gill, 1982), which lead to undulations in the mass field that are manifested as oscillatory signals at the fixed points where CTD and ADCP data are collected (Kundu, 1990). These baroclinic oscillations may be confounded with the internal tide signal if their period of oscillations are close to the tidal periods. In addition to these baroclinic oscillations, dynamic internal waves with periods shorter than the tidal one may be generated in the surrounding continental shelf break. As we will see, an EOF analysis may help separate these different contributions in the recorded signal. The identification of the EOF corresponding to the tidal signal was performed by application of least squares harmonic analysis at the frequencies of tidal constituents M_2 and K_1 , on the time sequence of

EOF amplitudes $a_j(t)$. Then, the EOFs whose temporal amplitudes showed a good fit to the harmonic signals M_2 and K_1 (correlation coefficients equal to or greater than 0.8) were included in summation (1) to reconstruct the internal tide. Similarly, EOFs related to shorter period internal waves were analysed by least-squares harmonic analysis. Their period was determined by comparing the waves to synthesised time series of different periods and selecting the period that produced the best fit between both series.

3.2. Dynamical mode decomposition

Once the time scale of interest was isolated from the original record, the next step in the analysis was the application of dynamical mode decomposition (DMD). DMD consists of the decomposition of the signal into vertical modes subject to the physical laws dictated by the hydrodynamic equations, as opposed to EOF analysis, which is solely determined by the statistical behaviour of the data. This technique provides (i) a more objective way than EOF to separate barotropic and baroclinic oscillations in the records, (ii) a filter procedure to remove spurious baroclinic signals from the record. This is of particular importance in this study due to the shortness of the time series of available data and to the rather rough sampling interval, and (iii) useful parameters to determine the spatial scales (i.e. wavelength) of the internal waves under study. A short description of the fundamentals of DMD technique and the manner it has been implemented in our analysis procedure is presented next.

Let us consider the hydrodynamic equations for the two-dimensional non-rotating fluid, with the additional assumptions of horizontally unbounded fluid, linear and Boussinesq approximations, negligible dissipative effects, flat bottom and homogeneous background stratification. The governing equations of motion are written as:

$$\frac{\partial u}{\partial t} = -\frac{1}{\rho_0} \frac{\partial p}{\partial x}, \quad (2a)$$

$$\frac{\partial w}{\partial t} = -g \frac{\partial}{\partial z} - \frac{1}{\rho_0} \frac{\partial p}{\partial z}, \quad (2b)$$

$$\frac{\partial \rho}{\partial t} - \frac{\rho_0 N^2 w}{g} = 0, \quad (2c)$$

$$\frac{\partial u}{\partial x} + \frac{\partial w}{\partial z} = 0, \quad (2d)$$

where u and w are the horizontal and upward vertical component of the perturbation velocity in a cartesian co-ordinate system (x, z) , p and ρ are the perturbations of pressure and density, ρ_0 is a reference sea water density:

$$N(z) = \sqrt{-\frac{g}{\rho_0} \frac{d\bar{\rho}(z)}{dz}}$$

is the buoyancy frequency, and $\bar{\rho}(z)$ is the undisturbed density profile. Since we are interested in cross-shore motions, x -axis points to the shore, that is, northwards.

Let us define the stream function ψ :

$$u = \frac{\partial \psi}{\partial z}, \quad (3)$$

$$w = -\frac{\partial \psi}{\partial x} \quad (4)$$

and assume normal mode solutions to the set of Eqs. (2)–(4) of the form:

$$(\rho, p, \psi) = [\hat{\rho}(z), \hat{p}(z), \hat{\psi}(z)] e^{i(kx - \omega t)}. \quad (5)$$

The following equation for $\hat{\psi}$ is then obtained:

$$\left[\frac{\omega^2}{\omega^2 - N^2} \right] \frac{d^2 \hat{\psi}}{dz^2} = k^2 \hat{\psi}, \quad (6)$$

which along with the boundary conditions at the surface ($z = D$) and bottom ($z = 0$):

$$\hat{\psi}(z = D) = 0; \quad \hat{\psi}(z = 0) = 0 \quad (7)$$

constitute a Sturm–Liouville problem with eigenvalues k_n^2 . The solution for a given ω is a linear superposition of a set of eigenfunctions $\hat{\psi}_n(z)$, or vertical modes, satisfying the orthogonality condition

$$\int_0^D \hat{\psi}_n(z) \hat{\psi}_m(z) dz = \delta_{nm}, \quad (8)$$

where δ_{nm} is the Kronecker delta.

Once the vertical structure of the stream function is determined, we fit the density and velocity observations to a linear combination of vertical modes:

$$\rho(x, z, t) = N^2 \sum_{n=1}^M \Gamma_n(x) \hat{\psi}_n(z) \cos[\omega t - \varphi_n^\rho(x)], \quad (9)$$

$$u(x, z, t) = \sum_{n=0}^M \gamma_n(x) \frac{d}{dz} [\hat{\psi}_n(z)] \cos[\omega t - \varphi_n^u(x)], \quad (10)$$

where Γ_n , γ_n , φ_n^p and φ_n^u are parameters to be determined from the fitting, $n = 0$ is the barotropic mode, and M is the number of the considered baroclinic modes.

Individual modes propagate only horizontally according to Eq. (5) but their superposition defines a perturbation that can propagate in both horizontal and vertical directions. This property is important in order to interpret the results of our analysis.

A representative buoyancy frequency profile that characterises the undisturbed state of stratification is needed in order to compute the vertical modes. We assume that N is only a function of depth, that is, the buoyancy profile is uniform along x at a fixed depth. Previously, a mean density profile is computed by fitting the time-averaged density profiles taken at the canyon head to the smoothed function:

$$\bar{\rho}(z) = \rho_s + a[(1 - e^{-b(D-z)})], \quad (11)$$

where D is the bottom depth. The fitting, illustrated in Fig. 2, is used to compute the buoyancy frequency profile $N(z)$ and, hence, the vertical

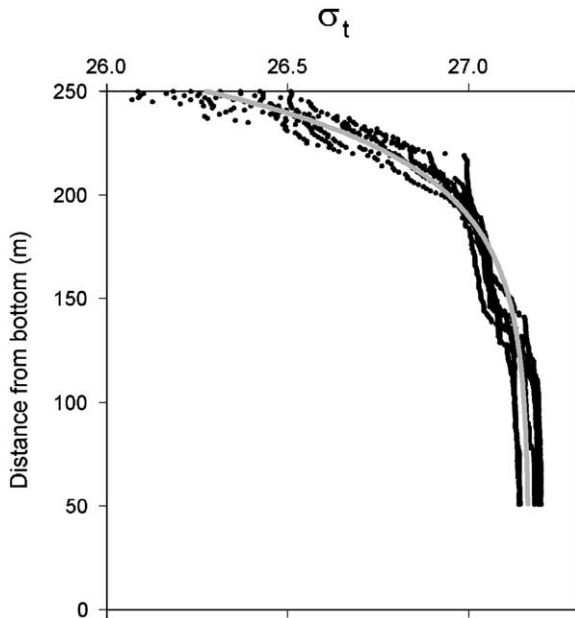


Fig. 2. Sigma-t recorded at E1 station during 24-h period (dots). The solid line is the curve resulting from the fit of the observations to the Eq. (11).

modes through Eqs. (6) and (7). The first six vertical modes are shown in Fig. 3.

3.3. CTD observations at the canyon head

CTD and ADCP data collected at the station in the mouth of Portimao Canyon did not show important internal oscillations in the first 200 m (maximum depth reached by the CTD). On the contrary, the station at the head of the canyon showed clear evidence of baroclinic oscillations. For this reason, we will centre our analysis of density oscillations on the region around the canyon head.

3.3.1. EOF analysis

Density data, originally sampled with vertical resolution of 1 m, were decimated to a sample each 10 m prior to EOF analysis. Fig. 4 illustrates the internal tide signal for the first five levels isolated by the analysis. The signals have been synthesised using five EOFs, which, jointly, explain about 90% of the density variance between 20 and 200 m. In order to explain the remaining variance at the most superficial levels an additional sixth EOF is needed. This EOF seems to be related to changes in the density of the near surface waters due to lateral excursions of frontal structures. Fig. 4 suggests that the internal tide near the canyon head has maximum amplitude of density perturbations between 30 and 50 m.

3.3.2. Fitting to dynamical modes

The internal tide signal isolated by EOF analysis is fitted to the vertical dynamical modes determined in the DMD analysis (Fig. 3) according to Eq. (9). Only the first five vertical modes were included in the analysis because the inclusion of an additional mode did not improve the fit. The density perturbation due to internal tide at a fixed point x_0 is

$$\rho(x_0, z, t) = N^2 \sum_{n=1}^M f_n(t) \hat{\psi}_n(z). \quad (12)$$

The fitting of each profile to Eq. (12) provides the time sequences $f_n(t)$ for each of the M vertical modes included in the analysis. The time sequences $f_n(t)$ are fitted to the functions

$$\Gamma_n \cos(\omega t - \varphi_n^p),$$

in order to estimate the parameters Γ_n and φ_n^p . Once this is done, we can express Eq. (9) as

$$\rho(x_0, z, t) = A_\rho(z) \cos[\omega t - P_\rho(z)], \quad (13)$$

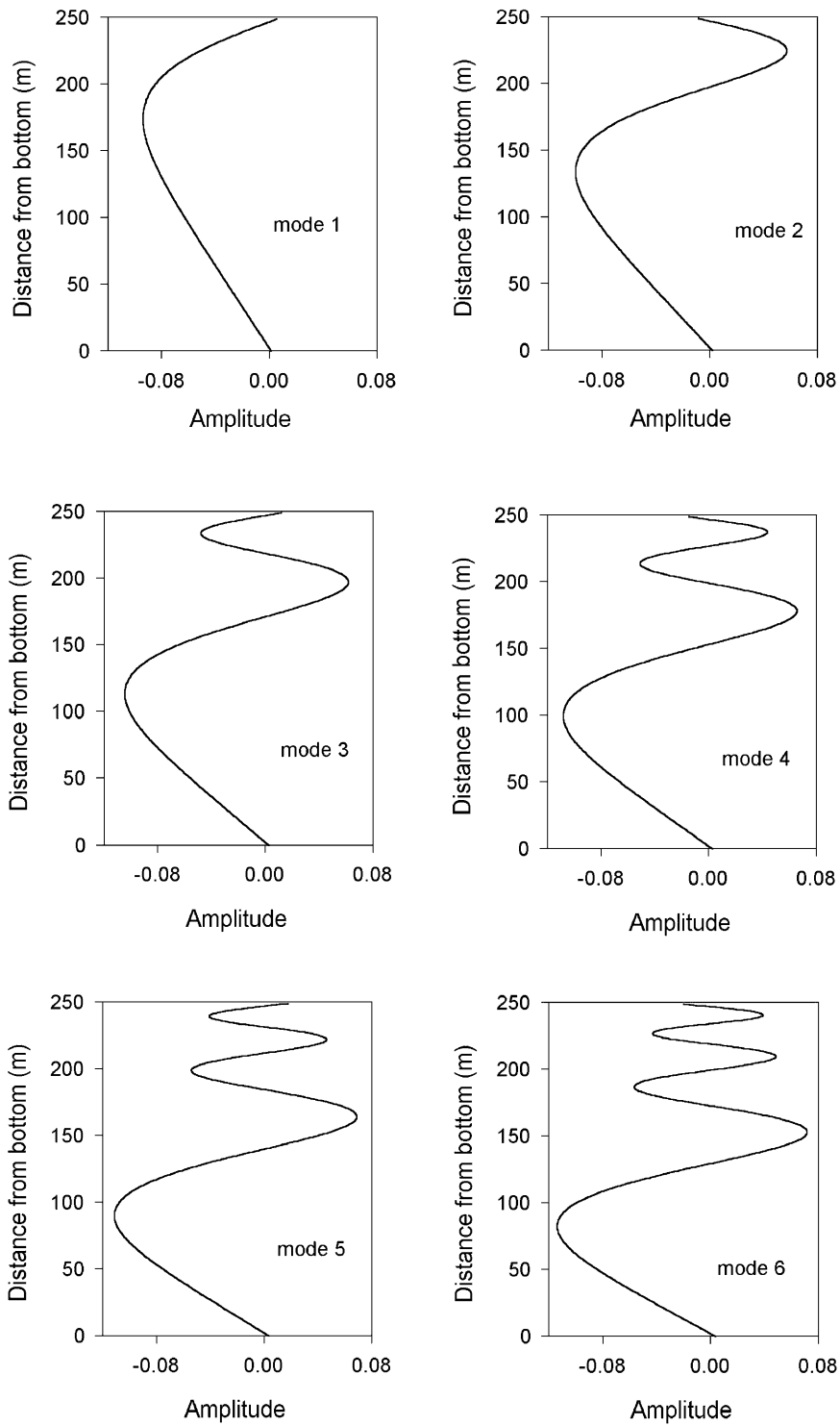


Fig. 3. Vertical dynamical modes for the stream function amplitude $\hat{\psi}(z)$, using the stratification deduced from the density profile shown in Fig. 2.

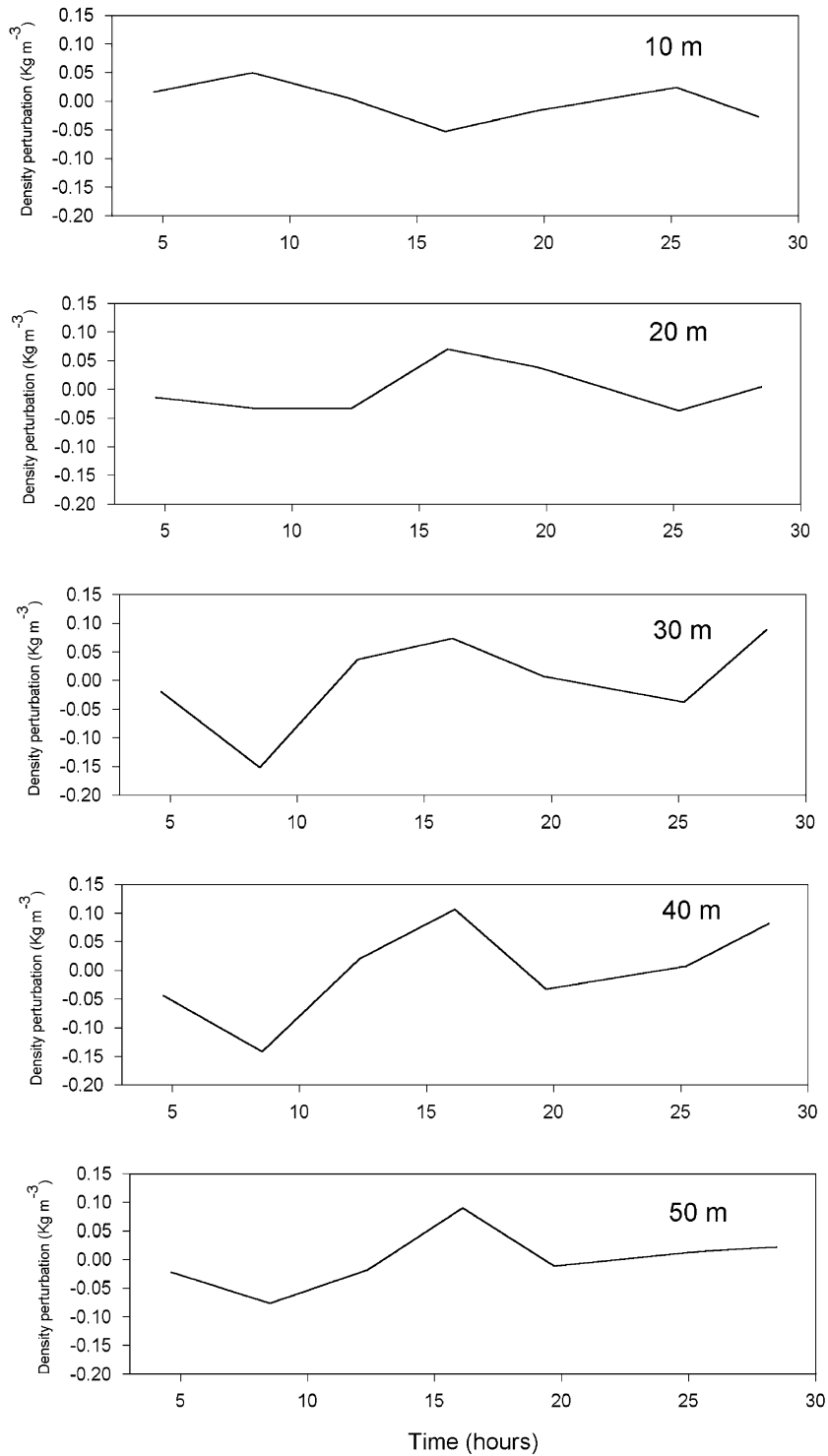


Fig. 4. Internal tide signal in the density oscillation at different depths at station E1, synthesised from EOF analysis results. GMT time origin is 5/27/2001 at 17:10.

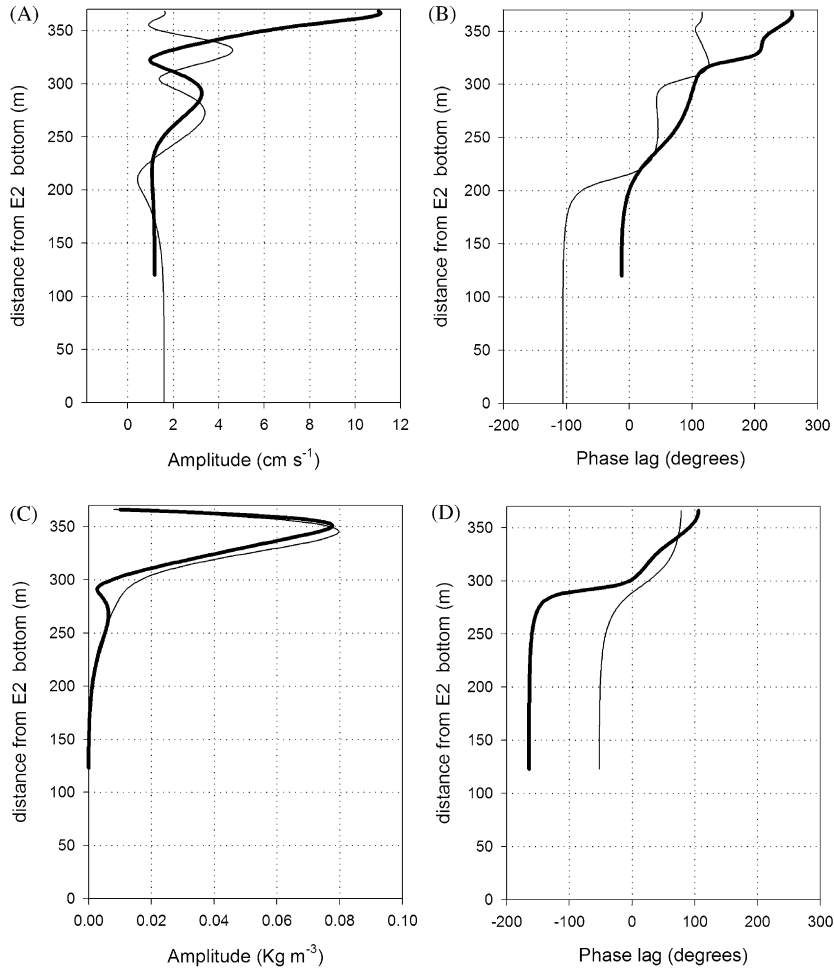


Fig. 5. Amplitude and phase lag profiles of semidiurnal internal tide at stations E1 and E2 (see text for details). The frequency of the semidiurnal tidal signal is assumed to be that of the M_2 constituent. (A) Amplitude of the horizontal velocity at E1 (thick line) and E2 (thin line). (B) Phase lag of the horizontal velocity at E1. (thick line) and E2 (thin line). (C) Amplitude of density oscillation at station E1. Thick line is the direct estimate from the density data and the thin line is the amplitude inferred from Eqs. (2c) and (2d) using the velocity profiles of panels (A) and (B). (D) Phase lag of the density oscillations at station E1. Thick line is the direct estimate from density data and the thin line is the phase lag inferred from Eqs. (2c) and (2d).

where

$$A_\rho(z) = N^2 \sum_{n=1}^M \Gamma_n \hat{\psi}_n(z), \quad (14)$$

$$P_\rho(z) = a \tan \left(\frac{\sum_{n=1}^M \Gamma_n \hat{\psi}_n(z) \sin \varphi_n^\rho}{\sum_{n=1}^M \Gamma_n \hat{\psi}_n(z) \cos \varphi_n^\rho} \right), \quad (15)$$

are, respectively, the depth-dependent amplitude and phase lag of the density perturbation associated with the internal tide of frequency ω . Fig. 5 shows both of them for the frequency of the main semidiurnal constituent M_2 . The maximum amplitude is achieved around 50 m depth.

The amplitude of the vertical displacement of the water parcels matching this density perturbation is computed integrating Eq. (2c) to obtain

$$\zeta(x_0, z, t) = \frac{g\rho(x_0, z, t)}{\rho_0 N^2}, \quad (16)$$

which, with the help of Eq. (13) gives

$$A_\zeta(z) = \frac{g}{\rho_0 N^2} A_\rho(z). \quad (17)$$

This equation relates the amplitude of isopycnal displacements originated by the internal tide to the amplitude of the density perturbation. With the density amplitude shown in Fig. 5, the maximum

amplitude of the semidiurnal vertical oscillation of density surfaces is around 15 m.

Phase lags decrease from surface to bottom, particularly at depths around the depth of maximum amplitude. This implies an upward phase propagation of the internal tide, which in turn implies downward energy propagation (the group velocity has negative vertical component). Velocity records analysed in the next section will reveal whether the horizontal component of the group velocity is directed shoreward or seaward.

3.4. Current velocity observations

This section analyses the current velocities acquired by the vessel-mounted 150-KHz ADCP. We will focus on two stations: E1, very close to the canyon head, and E2, 7 km seaward from the canyon head, in the along-canyon direction (Fig. 1). The ADCP velocities extend from 16 m down to 200 m depth at station E1, and to 350 m depth at station E2, with a vertical resolution of 8 m. Velocity time series have greater time resolution than density series because velocity profiles were acquired whenever the vessel passed over E1 and E2 in its way to the fixed CTD station. For this reason, the resulting sampling interval ranged from 35 min to 3.5 h.

3.4.1. EOF analysis

A vectorial EOF analysis was applied to the time series of east and north components of the ADCP velocities. Velocity data are represented by the complex number $s(z, t) = v_e(z, t) + iv_n(z, t)$ whose real and imaginary parts are the east ‘ v_e ’ and north component ‘ v_n ’, respectively. In the complex version of the analysis, the EOFs $e_j(z)$ and the temporal amplitudes $a_j(t)$ are complex functions and Eq. (1) adopts the form

$$s(z, t) = \sum_{j=1}^M E_j(z) e^{i\theta(z)} A_j(t) e^{i\phi(t)}, \quad (18)$$

where E_j and $\theta(z)$ are, respectively, the modulus and phase of the complex EOF $e_j(z) = e_j^R(z) + ie_j^I(z)$, and $A_j(t)$ and $\phi(t)$ are, respectively, the modulus and phase of the complex temporal amplitude, $a_j(t) = a_j^R(t) + ia_j^I(t)$. When the contribution of a given EOF to the velocity is nearly along a unique direction, the imaginary part of $a_j(t)$ is dropped and the expression for that EOF simplifies to

$$s_j(z, t) = E_j(z) a_j^R e^{i\theta(z)},$$

where $E_j(z) a_j^R$ is a scalar quantity that represent the projection of the current velocity associated with the EOF on the prevailing direction of the current, which is given by the angle $\theta(z)$ (measured anticlockwise from the east direction). Our data show that the EOFs of the current velocity are fairly colinear, and therefore the scalar approach is good for our purposes.

EOF analysis has been able to isolate two well-differentiated sources for the current velocity oscillations: internal tide on the one hand, and a shorter than tidal period (around 3.8 h) internal wave, on the other. Figs. 6 and 7 show both types of oscillations at five depth levels in the stations E1 and E2. To synthesise the internal tide signal we have used two EOFs at station E1 and three EOFs at station E2. In the case of the signal related to the shorter-period internal wave, only one EOF was needed at both stations.

3.4.2. Fitting to dynamical modes

The velocity series associated with the internal tide and with the shorter-period internal waves isolated by EOF analysis are fitted to the vertical dynamical modes determined in the DMD analysis (shown in Fig. 3) following Eq. (10). Note that now the basis functions are the derivatives $d\psi_n/dz$.

Only the first five vertical modes were included in the analysis of the internal tide, as including additional modes did not improve the fit. For the shorter period internal waves only the first three modes were needed. The velocity perturbation due to internal waves at a fixed point x_0 is

$$u(x_0, z, t) = \sum_{n=1}^M f_n(t) \frac{d}{dz} [\hat{\psi}_n(z)] \quad (19)$$

and the fitting of each velocity profile to Eq. (19) gives the time series $f_n(t)$ for each vertical mode included in the analysis. These series are fitted to the functions

$$\gamma_n \cos(\omega t - \varphi_n^u),$$

in order to estimate the parameters γ_n and φ_n^u . Eq. (10) is then expressed as

$$u(x_0, z, t) = A_u(z) \cos[\omega t - P_u(z)], \quad (20)$$

where

$$A_u(z) = \sum_{n=1}^M \gamma_n \frac{d}{dz} \left[\hat{\psi}_n(z) \right], \quad (21)$$

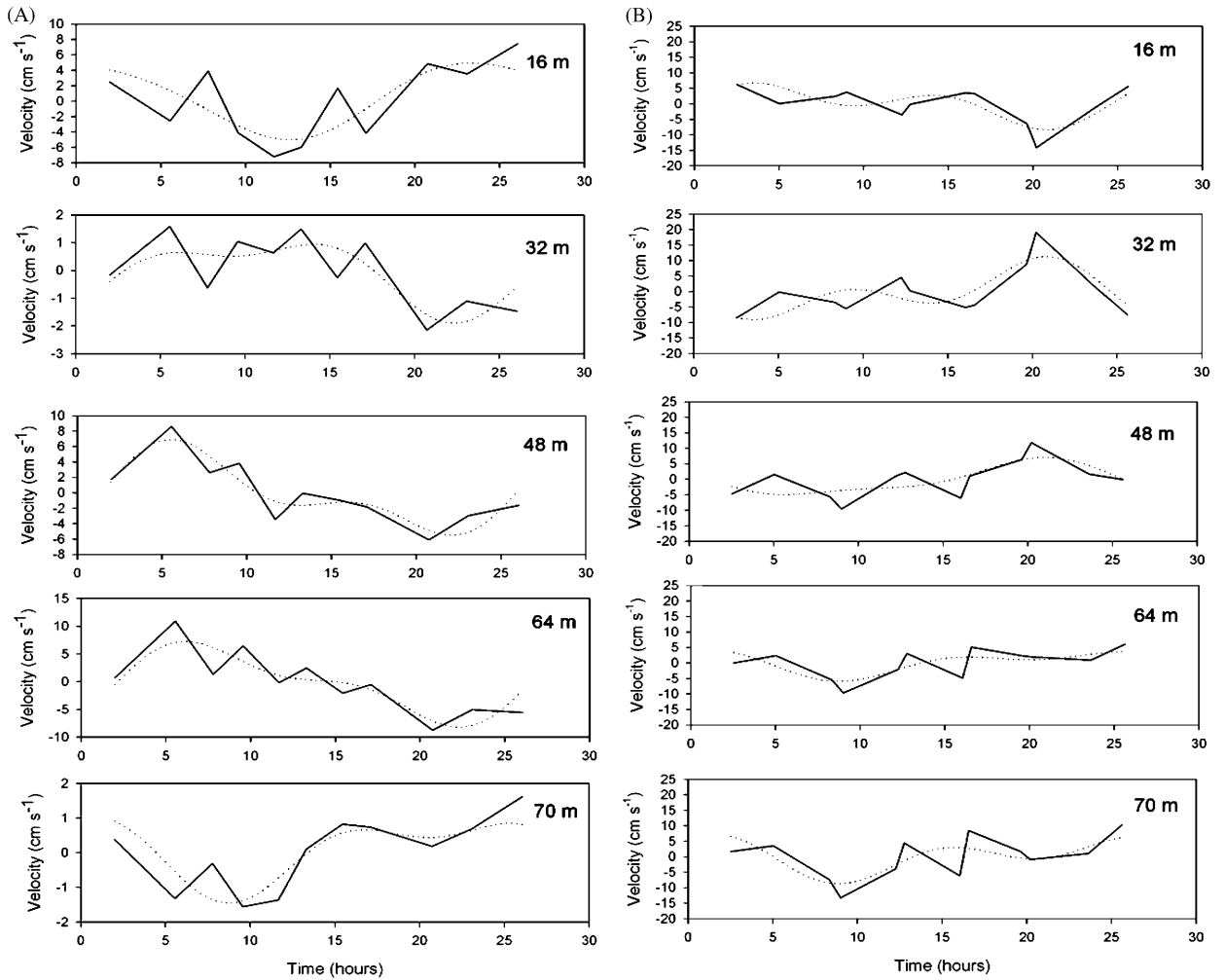


Fig. 6. (A) Internal tide oscillation of the horizontal velocity at different depth levels in station E1, synthesised from EOF analysis (solid line). Dotted line is the prediction using the amplitude and phase lag of K_1 and M_2 constituents determined by the least-squares harmonic analysis. GMT time origin is 5/27/2001 at 17:10. (B) The same as (A) for station E2.

$$P_u(z) = a \tan \left(\frac{\sum_{n=1}^M \gamma_n \frac{d}{dz} [\hat{\psi}_n(z)] \sin \varphi_n^u}{\sum_{n=1}^M \gamma_n \frac{d}{dz} [\hat{\psi}_n(z)] \cos \varphi_n^u} \right). \quad (22)$$

3.4.3. Internal tide signal

Panels A and B of Fig. 5 show the amplitude and phase lag of the semidiurnal oscillations in the current velocity at stations E1 and E2. Maximum amplitude is reached near the sea surface (around 10 m) at E1 and around 70 m at E2. At station E1 the phase lag decreases with depth throughout the water column, in agreement with the analysis of the density signal related to internal tide. It confirms the upward phase propagation of the internal tide and the downward component of the group velocity and

energy propagation. On the contrary, at E2 the phase lag increases slightly with depth around the level of maximum amplitude (Fig. 5A,B). This behaviour indicates an upward energy propagation within this depth range at this location.

These results can be analysed in terms of the characteristic lines (ray paths) of the internal tide propagation. According to linear theory of internal waves, the slope of the characteristic is

$$c = \pm \left(\frac{\omega^2}{N^2 - \omega^2} \right)^{1/2}. \quad (23)$$

The shape of the sea bottom along the axis of Portimao canyon shows three differentiated regions

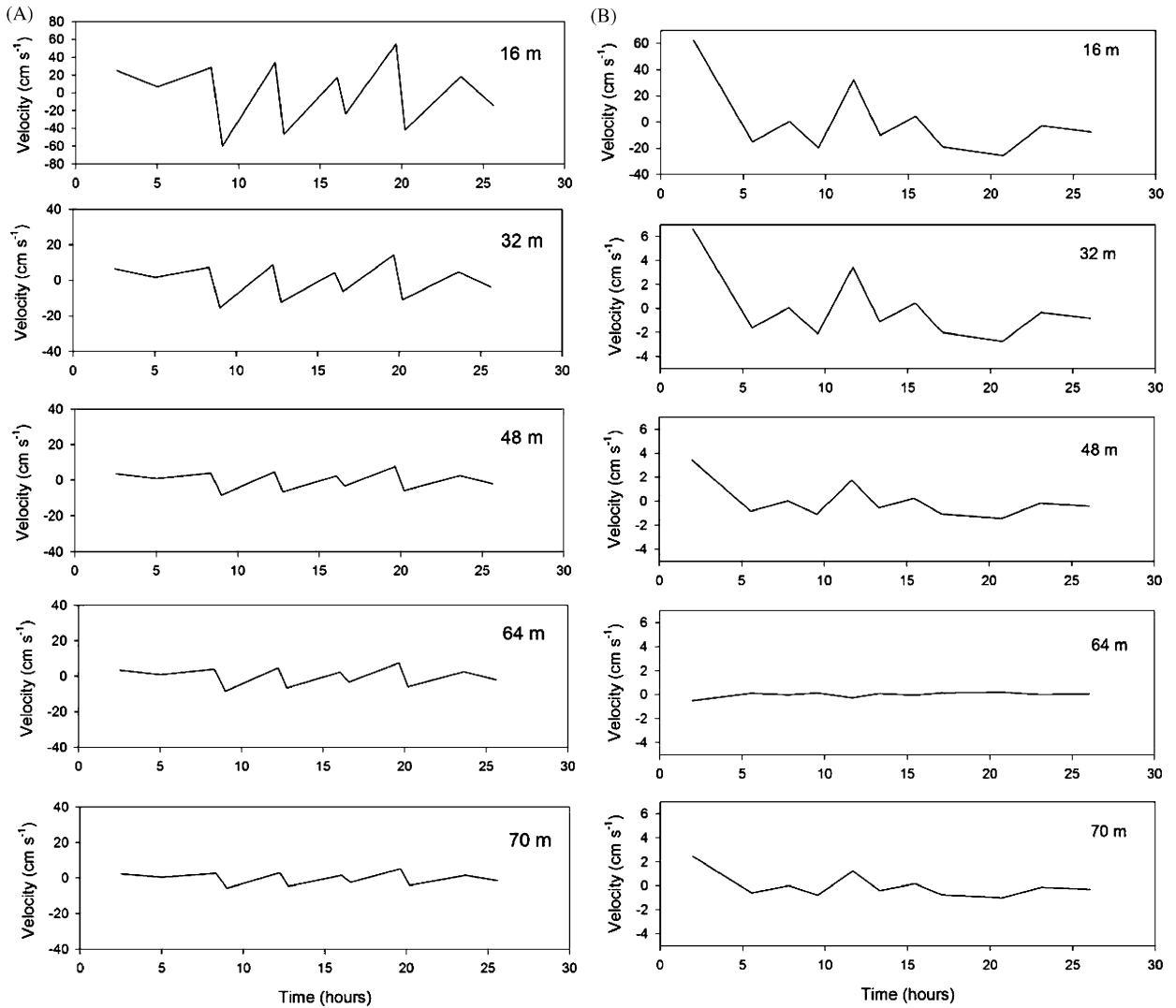


Fig. 7. (A) Shorter than tidal period internal-wave oscillation of the horizontal velocity (horizontal component) at various depths in station E1, synthesised from EOF analysis results. GMT time origin is 5/27/2001 at 17:10. (B) The same as (A) for station E2.

according to their bottom slope. The first and second regions in Fig. 8 are prone to generate internal tide, as bottom slope there is greater than (region 1) or near the same as (region 2) the slope of characteristics, respectively. In the steeper part of region 2, where the bottom slope becomes super-critical, the parameter beta is less than one, which implies seawards reflection of the internal tide. In region 1 the bottom slope is nearly critical, which allows internal tide energy to propagate both shoreward and seaward. Bottom slope in region 3 is much less than critical, so that this region is not suitable for generating internal tides.

The ray paths of the M2 internal energy, hypothetically generated in any of the two favourable regions, are shown in Fig. 8. They have been computed using the $N(z)$ profile corresponding to the density profile of Fig. 2. The pattern depicted by the different rays is rather complicated but, as a general description, rays generated in the shelf (region 1) and radiated seawards pass through station 1 after being reflected in the sea surface. They concentrate in the near surface layer and propagate downwards, both facts in good agreement with the results of amplitudes and phases of the internal tide at E1 deduced from the DMD

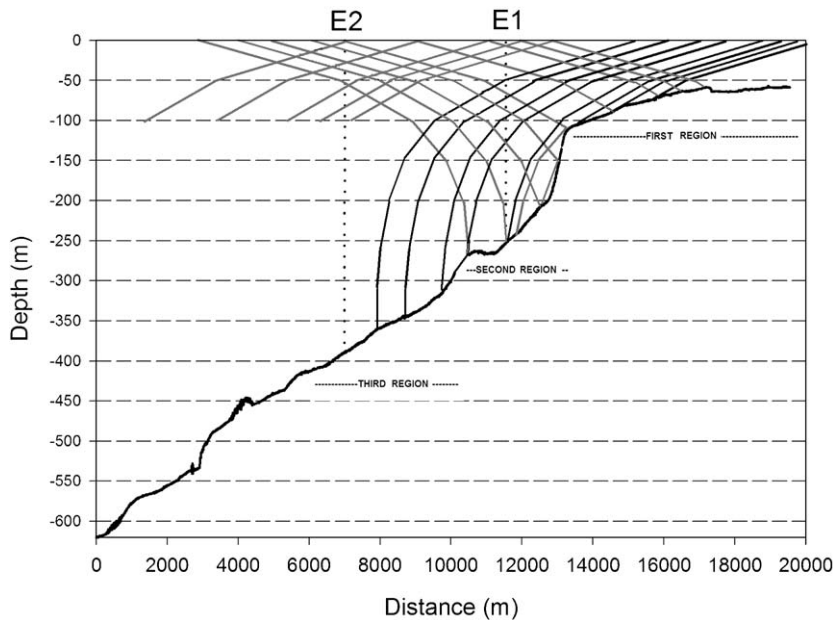


Fig. 8. Characteristic lines of the semidiurnal internal tide on a vertical section located along the main axis of the Portimao Canyon. Grey lines indicate beams progressing seaward, black lines indicate beams progressing shoreward.

analysis (Figs. 5A,B). Rays passing station E2 come from region 2, some of them after reflection in the supercritical bottom slope, and also from region 1. These latter rays would be weaker due to the energy dissipation that must have undergone while travelling from their source. Consequently, they would be less important than those coming from region 2. If so, the ray concentration and its upward propagation in the upper part of the water column at station E2 would again agree with the results from DMD analysis.

Eq. (23) can also be used to estimate the horizontal scale of the internal tide since the internal wave slope c is the ratio of the horizontal (k) and vertical (m) wavenumbers (Gill, 1982; Petrucio et al., 1998):

$$c = k/m. \quad (24)$$

Under the WKB approximation, the vertical wavenumber m can be estimated as the local vertical gradient of the phase, that is, $m = dP_u/dz$, which, according to Fig. 5, gives $m = 6.0 \cdot 10^{-2} \text{ m}^{-1}$ for the upper 50 m at station E1. Within this range of depths, Eq. (23) gives $c = 1.5 \times 10^{-2}$, which implies $k = 9 \times 10^{-4} \text{ m}^{-1}$, or a horizontal wavelength of around 7 km, which is of the order of magnitude of wavelengths obtained through the DMD analysis (Table 2).

Neither of these analyses being conclusive, they provide results which are physically compatible with the DMD decomposition carried out. This is important because the shortness of the time series analysed does not allow to extract statistically robust conclusions from the data. The relative good agreement of the results deduced from our data analysis with the predictions of analytical models is thus encouraging.

3.4.4. Shorter-period internal wave signal

Fig. 9 shows the amplitude and phase, referred to the origin of the time series, of the short period internal waves at stations E1 and E2 after fitting the signals to the dynamical modes. Maximum amplitude is achieved near the sea surface as in the case of the internal tide. Phases show an abrupt change of 180° in between the two maxima observed in the vertical structure of amplitudes. This result is consequence of the EOF processing used to separate out tidal and higher frequency oscillations in the velocity field, which used just the first EOF to reconstruct the higher-frequency part, as the inclusion of higher EOFs did not improve the fitting. We are aware that the synthesised series are not able to reproduce some of the features of the internal wave field but, as far as the first EOF accounted for most of the variance, the main global features should be

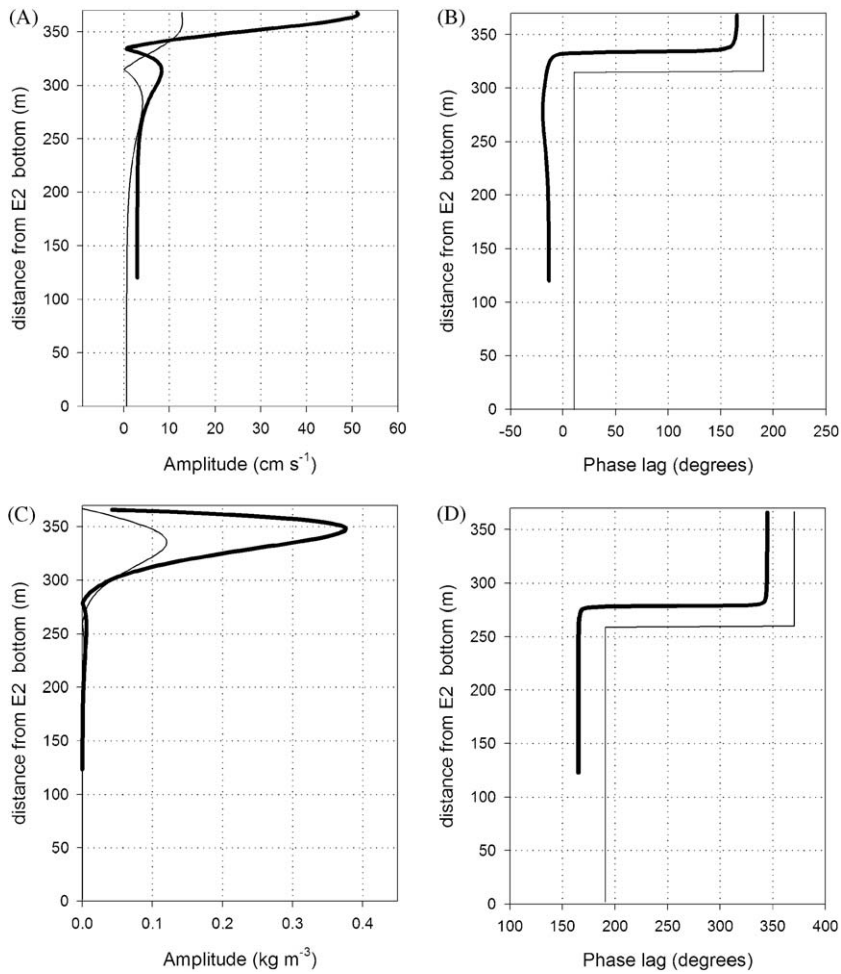


Fig. 9. Amplitude and phase lag of the shorter than tidal period internal waves at stations E1 and E2. (A) Amplitude of the horizontal velocity at E1 (thick line) and E2 (thin line). (B) Phase lag of the horizontal velocity at E1 (thick line) and E2 (thin line). (C) Amplitude of the density oscillations inferred from Eqs. (2c) and (2d), at E1 (thick line) and E2 (thin line). (D) Phase lag of the density oscillations inferred from Eqs. (2c) and (2d), at E1 (thick line) and E2 (thin line).

well captured by the reconstruction. We focus on two of these features: first, that the amplitude of these internal waves is much greater at E1 than at E2 (Fig. 9, see also Figs. 7A and B), and, second, that the phase increases from E1 towards E2, which implies seaward propagation of the perturbation. A likely scenario is that waves generated shoreward of station E1 (probably at the shelf break) progress in both directions, inshore and offshore.

Regarding the physical origin of these internal waves we have considered two possibilities: (1), they are the trailing waves of an internal bore generated over the continental slope and (2), they are generated by interaction of non-tidal barotropic flow with topography.

Internal bores form when the internal Froude numbers $F_n = U/c_n \geq 1$, U being the barotropic tidal

Table 1
Amplitude and phase lag of the barotropic current velocity isolated by the fitting to dynamical modes

Station	Amplitude (cm s ⁻¹)	Phase LAG (deg.)
<i>Barotropic tidal current (M₂)</i>		
E1	3.0	90.2
E2	1.2	278.6
<i>Barotropic shorter period wave current</i>		
E1	13.55	348
E2	—	—

Shorter period wave barotropic current is absent at station E2.

current and c_n the phase speed of baroclinic mode n (Holloway, 1987). Tables 1 and 2 show that U is much less than any of the phase velocities for the first baroclinic modes. We conclude that internal

Table 2
Wavelength and phase speed of the first three baroclinic modes resolved by the dynamical modes decomposition analysis

Baroclinic mode	Wavelength (m)	Celerity (cm s ⁻¹)
<i>Internal semidiurnal tide</i>		
1	16,036	36
2	7593	17
3	4982	11
<i>Shorter period internal wave (T = 3.8 h)</i>		
1	5331	38
2	2520	18
3	1652	12

bores are not expected to be formed in the area and therefore neither are the trailing waves associated with the disintegration of the bore.

Regarding other possible mechanisms, likely candidates for barotropic forcing are the barotropic waves trapped in the continental shelf (trapped shelf waves, TSW), such as the barotropic edge waves of 1–4 h periods observed around New Zealand continental shelves (Goring and Henry, 1998), whose shape is similar to the shape of the continental shelf of the Gulf of Cádiz.

To explore the possibility of TSW, we use the model developed by Mysak (1980). The model assumes a straight coast with a shelf of constant slope and an abrupt change of depth at the shelf break. More specifically, the sea bottom is given by

$$H(x) = \frac{d}{L}x \quad 0 < x < L,$$

$$H(x) = D \quad L < x < \infty,$$

where x is the across-shelf coordinate increasing seaward from the coast line ($x = 0$), d is the depth at the shelf edge and D is the depth in the deep region.

The dispersion relation for the barotropic waves trapped by this across-shelf topography may be written in terms of the Laguerre Function (Mysak, 1980) as

$$L_v(2kL) = 0, \quad (25)$$

where k is the along-shore wave-number and v is given by

$$v = \left[\frac{f}{2\omega} + \frac{(\omega^2 - f^2)L}{2d g k} \right]^{1/2} - 0.5. \quad (26)$$

For $L = 40$ km and $d = 100$ m, which are values representative of our area, and for a period

$T = 3.8$ h, Eqs. (25) and (26) predict a wavelength of the order of 230 km, which results a value too large to be allowed by the coast line extension of the Gulf of Cádiz. Therefore, we have to conclude that the physical origin of the shorter period internal waves remains unclear and that further analysis is needed to clarify this issue.

Some additional evidence for short period internal waves around the Portimao Canyon is provided by the temperature oscillation at 95 m measured by a thermistor chain moored on the shelf near the head of the canyon (see map on Fig. 1). Fig. 10A shows the spectral density of the original series, and Fig. 10B shows the spectral density of the de-tided series. A considerable part of the residual variance is found at shorter than tidal periods. Some peaks in the spectrum are possibly related to overtides but other peaks like those centred around 0.22, 0.36 and 0.40 cycles/h are not. They could be the signatures of the short period internal waves discussed in this section.

4. XBT and ADCP spatial observations

This section presents complementary information based on observations taken during the transit of the vessel along the main axis of the canyon with the aim of analysing the spatial features of the internal wave fields in order to confirm some of the results obtained in previous sections. Observations consisted of temperature profiles obtained from XBTs casts and ADCP velocities acquired as the vessel moved along the canyon axis. The time spent in the run was 81 min during which XBT were dropped every 3 min and ADCP velocities were sampled every minute. At the vessel speed, these temporal samplings produce spatial samplings of 360 and 120 m, respectively.

Fig. 11 shows the vertical section of temperature obtained from XBT casts along the canyon axis. The internal wave field is evident from the undulations of the isotherms, which show oscillation amplitudes higher than 10 m. These data have been processed to separate length scales greater and lower than 4500 m. The part with larger spatial scale is associated with the internal tide and the part of smaller spatial scale is associated with the shorter period internal waves. These associations are guided by the results of the analysis carried out on the time series at stations E1 and E2, which assigned wavelengths of the order of 5000–9000 m for the two first baroclinic modes

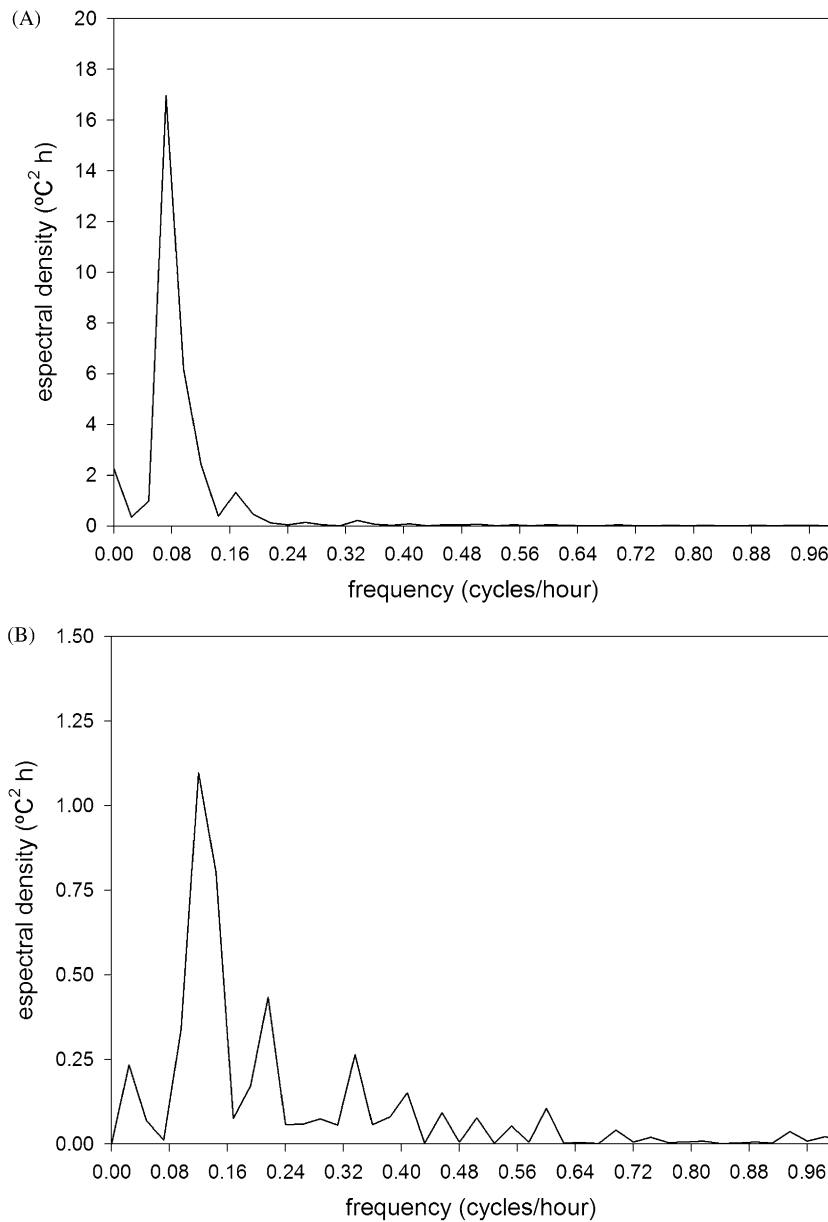


Fig. 10. (A) Spectral density of the temperature oscillations recorded, with a sampling interval of 1 min, during 42 h, at 95 m depth in location 'T' (see Fig. 1). (B) Spectral density of the de-tided temperature record. A minimum bandwidth of $\Delta\sigma = 0.024$ cph have been chosen, in order to achieve a better definition of the spectral peaks.

of the internal tide and 1500–4000 m for the three first baroclinic modes of the shorter period internal waves (Table 2). The temperature time series at 25 m (Fig. 11B) and the meridional velocity component at 32 m (Fig. 11C) indicate that the larger scale part contains spatial structures within the assigned range. The short scale part of the meridional velocity component (Fig. 11D)

contains also spatial structures that suggest shorter-period internal waves. As a general conclusion we remark that the spatial observations are compatible with the results inferred from the time series at the fixed stations and they provide a reasonable confidence on the actual existence of these two types of internal waves of well-differentiated periods.

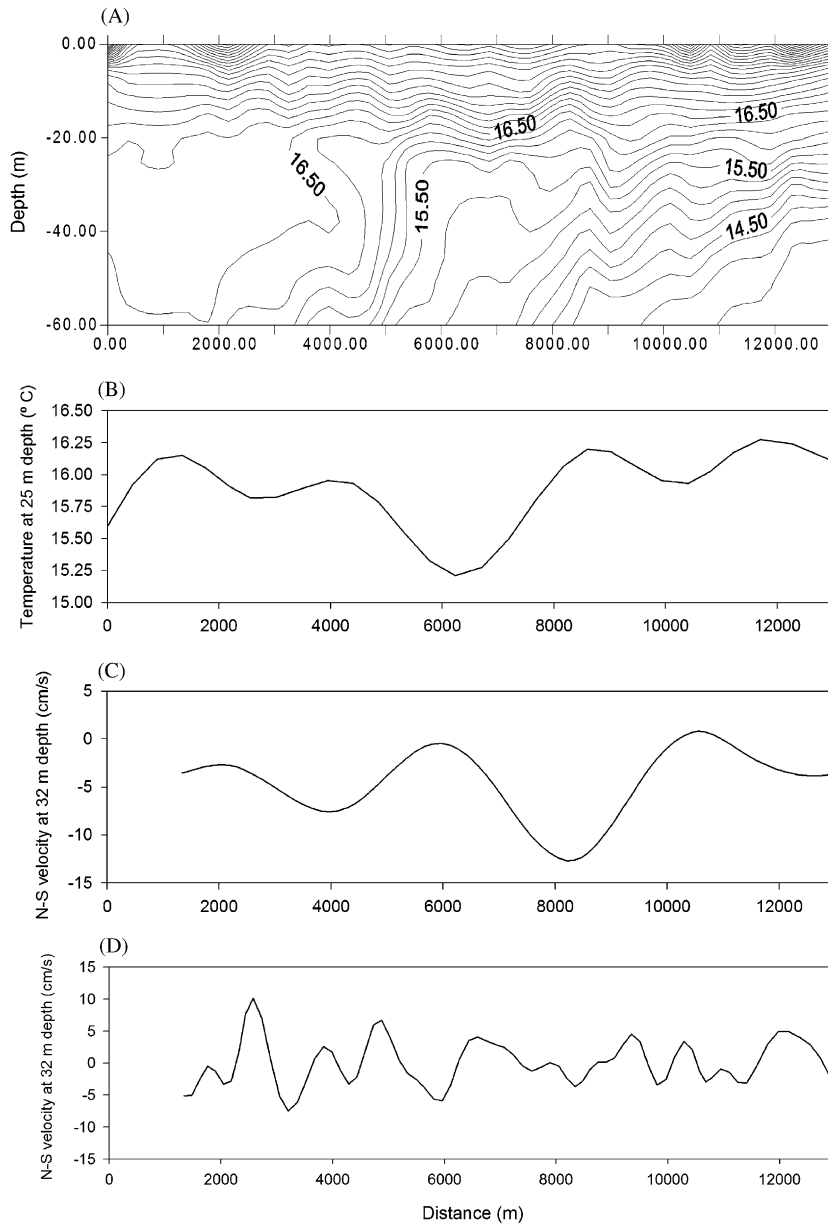


Fig. 11. (A) Vertical profile of temperature (°C) along the transect shown in Fig. 1. (B) Temperature signal at 25 m depth after removing the signal with wavelengths lesser than 4500 m. (C) Along canyon ADCP velocity at 32 m depth after removing the signal with wavelengths lesser than 4500 m. (D) Along canyon ADCP velocity at 32 m depth of wavelengths lesser than 4000 m.

5. Internal wave energetic and induced mixing processes

This section deals with energy aspects of the internal tide and shorter-period internal waves in the continental slope along the Portimao Canyon. The analysis is based on the results of Section 2 and

its objective is to estimate time variations of the total energy in order to infer energy fluxes from the generation region (the continental slope) both in the offshore and inshore direction. This energy flux is further considered as a possible source of available energy to accomplish mixing within the water column nearby the generation area.

5.1. Energy calculations

According to the linear theory of internal waves, the time variations of the total energy in a plane internal wave at a given position x_0 is

$$TE(x_0, z, t) = \frac{1}{4}\rho_0[u(x_0, z, t)^2 + w(x_0, z, t)^2] + \frac{1}{4}\frac{g^2}{\rho_0 N(z)^2}\rho(x_0, z, t)^2, \quad (27)$$

where the first and second term on the right-hand side are, respectively, kinetic and potential energy. Values of TE may be obtained using Eq. (13) for ρ , Eq. (19) for u and the relation $w = \partial\zeta/\partial t$ after using Eq. (16).

We define the potential energy anomaly of the water column between depths z_0 and z_1 as

$$\phi = \frac{g}{2(z_1 - z_0)}\rho_m(z_1^2 - z_0^2) - \frac{g}{(z_1 - z_0)}\int_{z_0}^{z_1}\bar{\rho}(z)zdz, \quad (28)$$

where the first term on the right-hand side represents the potential energy of the mixed water column, ρ_m being the mean (constant) density of the water column after mixing. The second term is the potential energy of the stratified water column before mixing, $\rho(z)$ being the mean profile along the water column. The magnitude ϕ is the amount of energy per unit volume necessary to fully mix the water column considered.

5.2. Mixing phenomena induced by internal waves

Estimates of TE computed from Eq. (27) for the M_2 internal tide and shorter period internal waves are shown in Fig. 12. The energy has been averaged over one M_2 tidal period for the internal tide and over 3.8 h interval for the shorter-period internal waves, respectively. These estimates have been explored to test whether or not they are sufficient to fully mix a given water column by converting the energy of the internal waves into potential energy through turbulent mixing.

Let us consider a portion of the water column 50 m thick located horizontally around the shelf break and vertically around the depths where the transition between upper (0–50 m) and slope (50–100 m) waters is expected to occur. Using Eq. (28) and the density profile of Fig. 2, we estimate a potential energy anomaly of $\phi = 13.7 \text{ J m}^{-3}$ for this portion of the water column

(25–75 m). This would be the amount of energy per unit volume necessary to mix slope and upper waters within the chosen water column.

Fig. 12 shows that TE of the internal tide is not enough to produce a full mixing the water column, even in the unrealistic case that all of its energy is transformed into potential energy by turbulent mixing. But the energy carried by the shorter-period internal waves recorded at station E1 could be large enough to do it. The conversion of wave energy into potential energy of the background flow by turbulent mixing depends on the mixing efficiency, which can be defined as the ratio ϕ/TE . This ratio, in stratified sheared flows, is about 0.2 (see Peltier and Caulfield, 2003, for instance), a value widely accepted in the literature although some authors give 0.15 or even less as an upper limit (Osborne, 1980).

Comparing the estimates of TE at stations E1 and E2, we conclude that more than 90% of the energy at E1 has been dissipated before reaching E2 (Fig. 12). A representative value of the depth-averaged TE within the upper 100 m of the water column at E1 is around 50 J m^{-3} , while it is an order of magnitude lower at E2. Most probably, this energy dissipates by turbulent mixing. If so, a rough estimation of the mixing efficiency could be given by $\phi/TE \approx 13/50 = 0.26$, which is not far from the empirical value of 0.2 observed in laboratory experiments. Therefore the short-period internal waves are potentially capable of producing important mixing in the vicinity of the Portimao Canyon's head. Under the hypothesis that these waves are generated shoreward of our observation sites, we do not discard the possibility that turbulent mixing is also produced shoreward of our stations, i.e. over the continental shelf, thus representing an important mechanism for water fertilisation.

A different approach to mixing can be done by means of the gradient Richardson number estimates (New, 1988; Bruno et al., 2002). This number is defined as

$$R_i(z) = \frac{N^2}{(\partial u/\partial z)^2},$$

where N is the buoyancy frequency of the undisturbed state and u is the velocity field associated with the motion under consideration. Using the vertical profiles of horizontal velocity shown in Figs. 5 and 9 for internal tide and shorter-period wave fields, respectively, and assuming a time

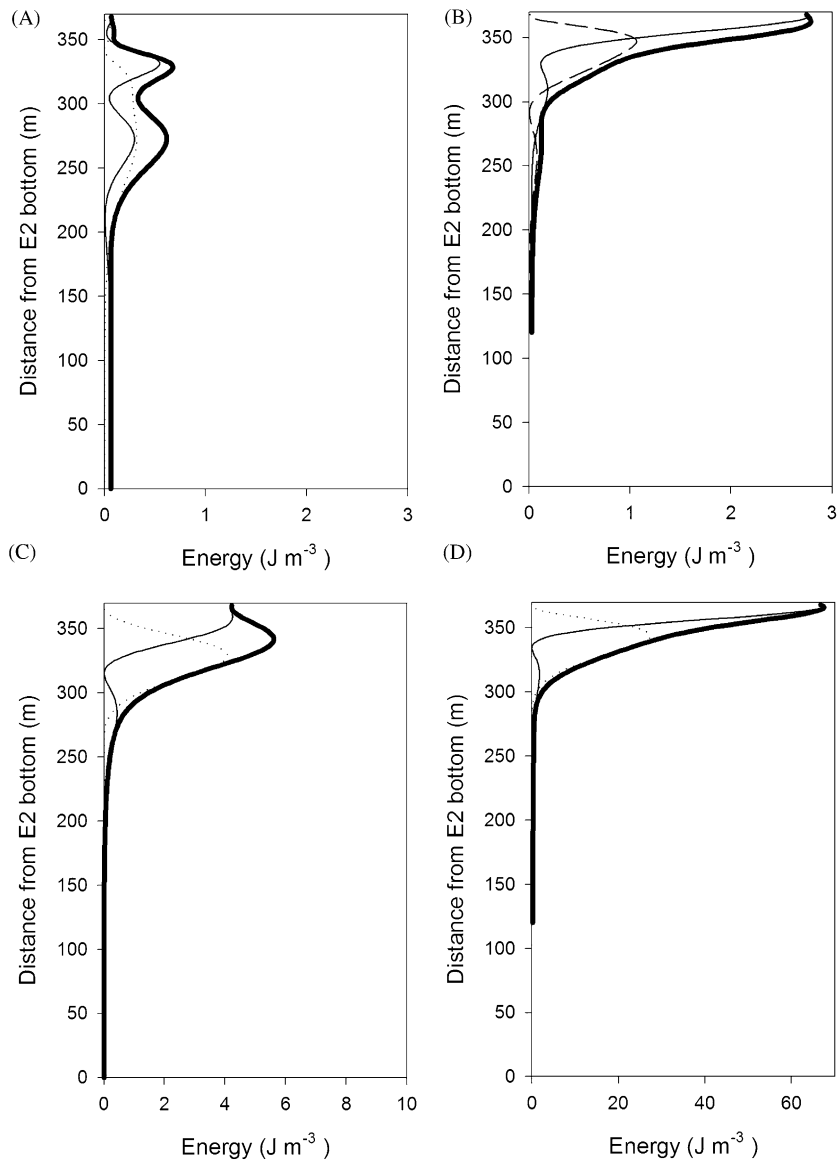


Fig. 12. (A) Internal wave energy, averaged over one period, for the internal tide at E2. (B) Same as (A) for station E1. (C) Internal wave energy averaged over 3.8 h, for the shorter period waves at E2. (D) Same as (C) for station E2. In all panels, the dotted line is potential energy, the thin line is kinetic energy and the thick line is total energy.

dependence given by Eq. (20), ω being either the frequency of the shorter period waves or that of M_2 , we can reproduce the time evolution of $R_i(z)$ during 12 h at stations E1 and E2 (Figs. 13 and 14). R_i is usually lower than the critical value 0.25 close to the sea surface at station E1, suggesting that mixing is expected to occur regularly in this portion of the water column. They are the short period internal waves that bring R_i below the critical value, internal tide playing a negligible role. At station E2, R_i does

not reach the critical value, although it is approached every 2 h (half of the internal wave period). As expected, critical or near-critical values of R_i at both stations E1 and E2 occur at depths where maximum amplitude of the internal wave oscillations is found (Fig. 9), which obviously coincides with the internal wave beams.

Fig. 15 shows two vertical cross-sections of R_i computed from CTD and ADCP observations along two transects near the Portimao Canyon area

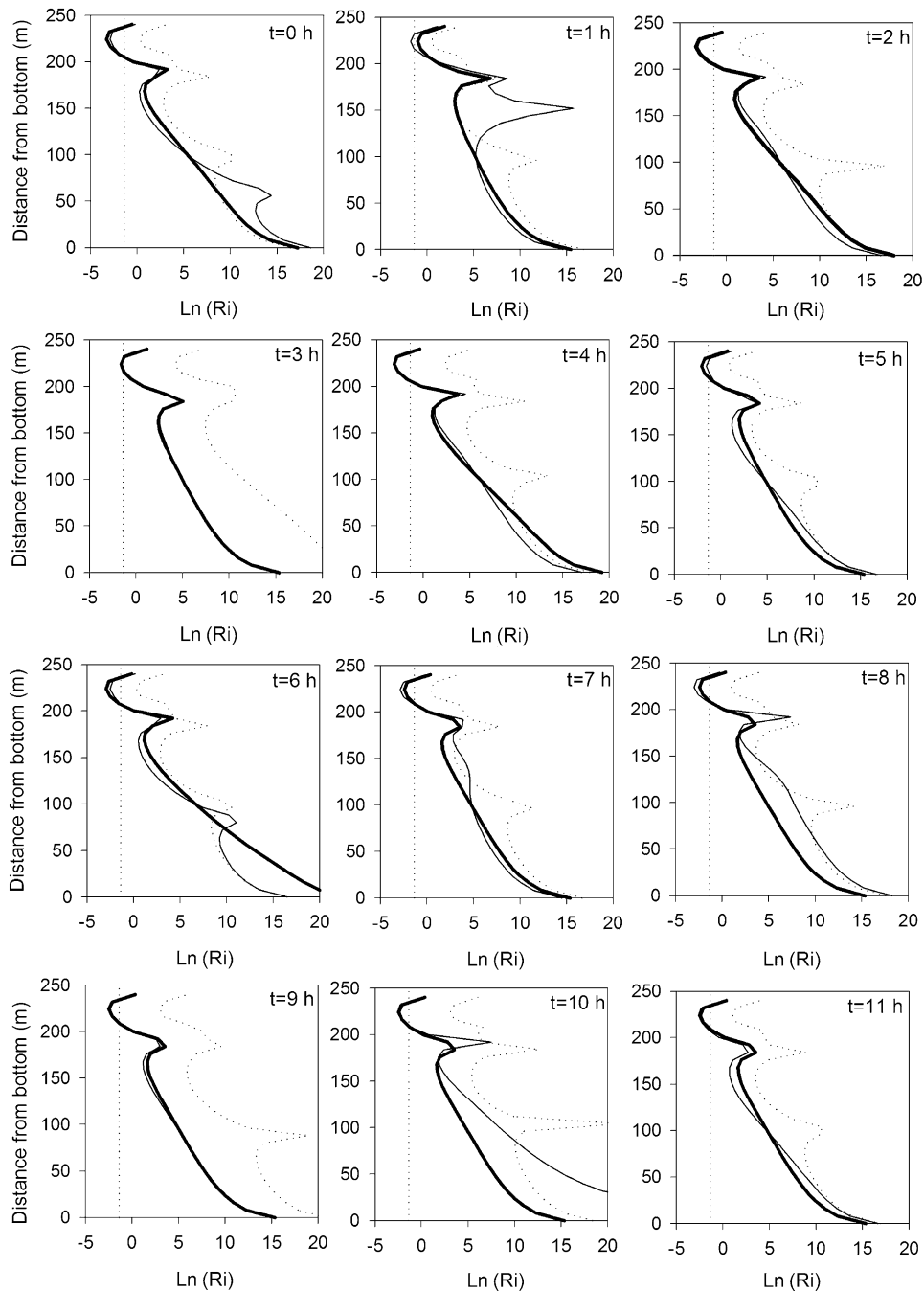


Fig. 13. Time evolution of the R_i profiles associated with internal waves during 12 h period at station E1. Dotted line is the contribution of the internal tide, thick line is the contribution of the shorter period internal wave, and thin line is their joined contribution. Vertical dotted line indicates the critical value $R_i = 0.25$.

but outside the canyon. Red colours, which correspond to regions of critical or near-critical R_i , suggest that mixing can potentially take place in many different spots and not only within the canyon. It is interesting to note that the patches of

yellow–red colours in Fig. 15 have a clear tendency to align along straight lines, which could be the manifestation of the internal wave beams according to our previous discussion. White lines in Fig. 15, plotted with some artistic licence, would represent

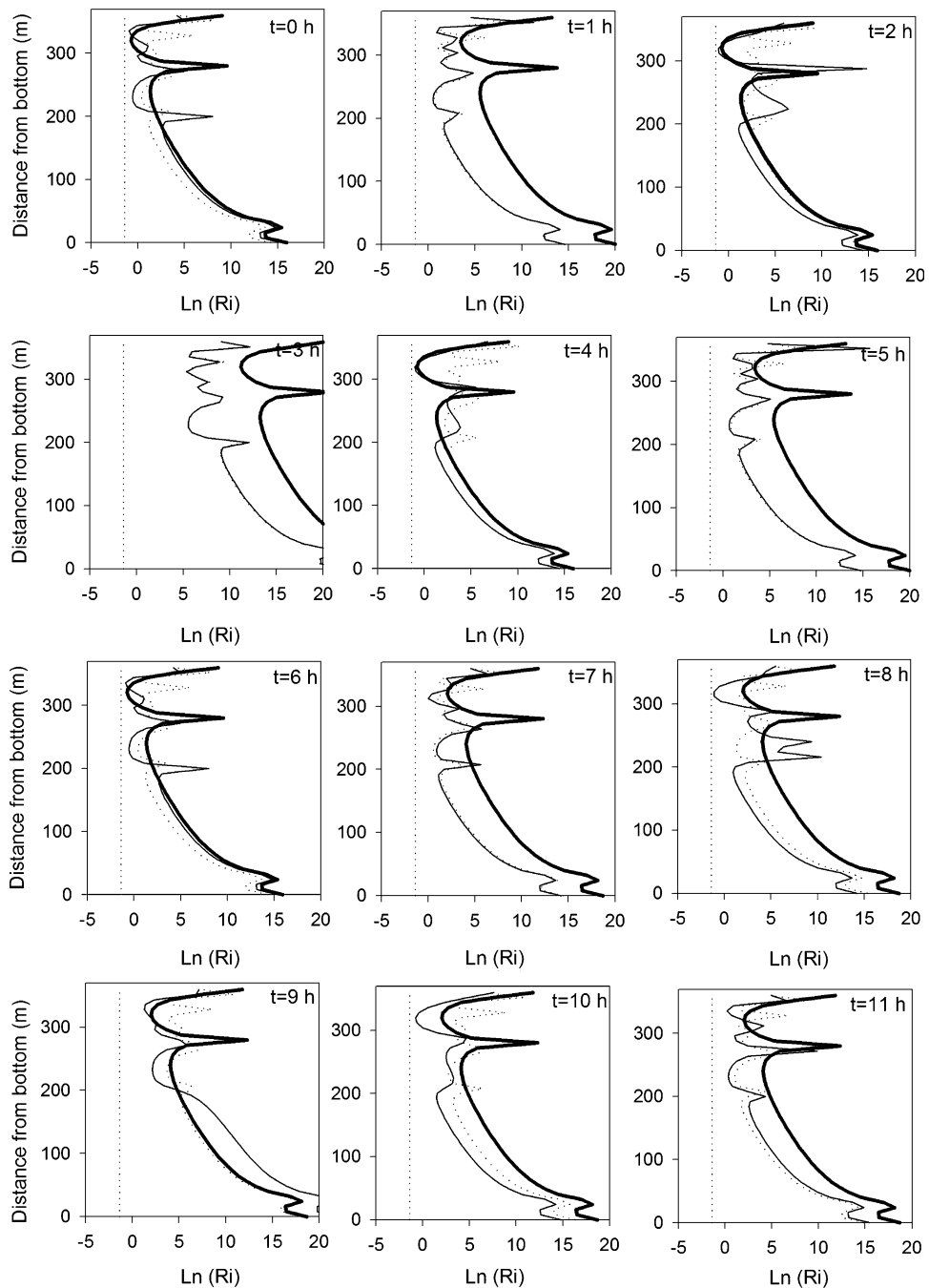


Fig. 14. Same as Fig. 13 for station E2.

some of these beams generated at the shelf break. The agreement between the patches of low R_i values and the beams is noticeable, particularly in the transect T1, suggesting that the mixing which can take place in this area is linked to internal waves. Our observations tend to support the hypothesis

that internal wave activity and induced mixing processes in the region around the Portimao Canyon area is a regular phenomenon. This phenomenon is able to accumulate relatively cold water around the shelf break and to form (or at least, to help maintain) a continental slope front and

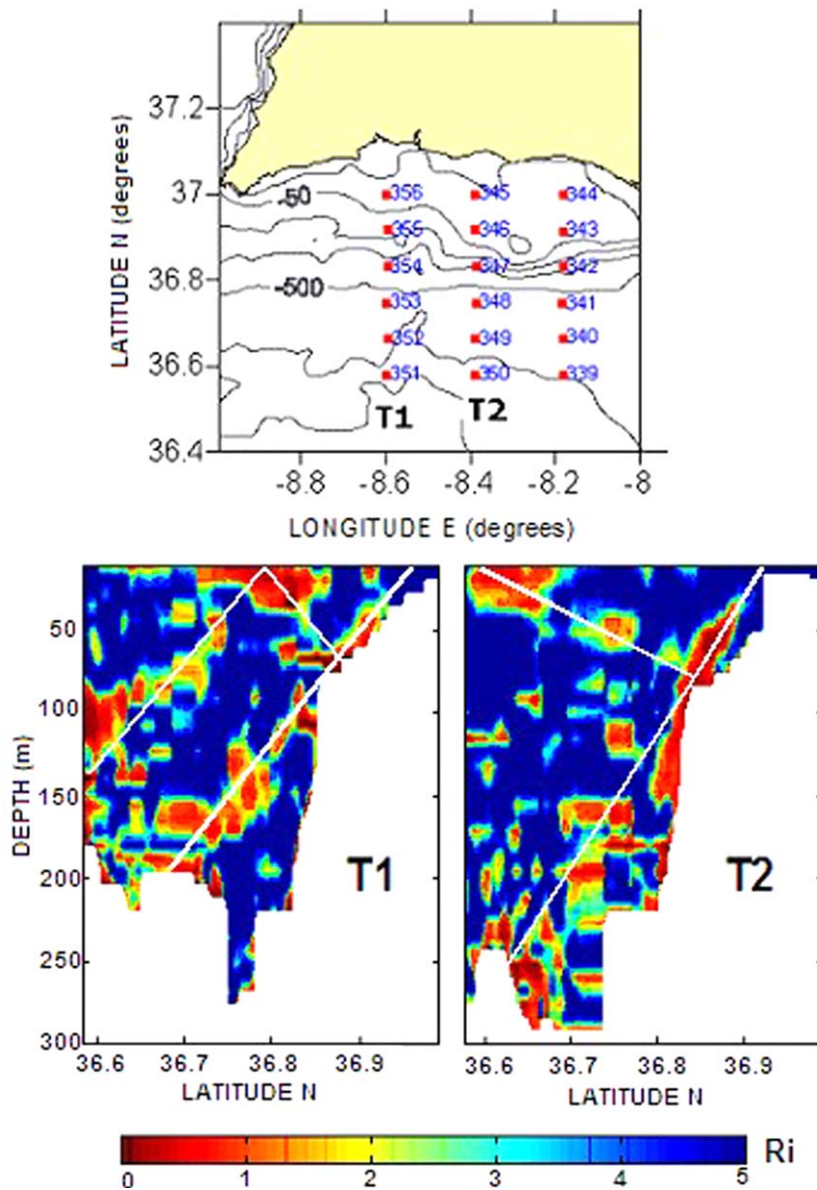


Fig. 15. Contours of R_i along the transects shown in the upper panel in the Portimao Canyon area. The white lines illustrate ray paths of internal energy emanating from the continental shelf break.

associated jet, which must flow westward. We put forward this rather speculative mechanism in order to explain the core of relatively cold water flowing over the continental slope toward the west reported in García-Lafuente et al. (2006).

6. Conclusions

Internal waves and their likely related induced mixing phenomena in the Portimao Canyon area, southern Portuguese coast, have been analysed. The

observations consisted of ADCP velocities and CTD measurements obtained during a 24-h period at two fixed stations located along the main axis of the canyon. The station closer to the shore is located near the canyon head, and the other 5 km seaward. These data sets are complemented with vertical cross-sections of temperature acquired by means of XBT casts along the axis of the canyon and with time series of temperatures recorded near the canyon head by a thermistor chain moored on the continental shelf. The processing of the time series

of velocity at two fixed stations, which was based on EOF (to filter out noise) and DMD analysis, showed the existence of two different types of internal waves: a rather clear internal tide signal and other internal oscillations whose characteristic period was shorter than that of tides.

An energy balance has been carried out to test whether or not the energy carried by the waves is enough to produce important mixing near the shelf. The internal tide is clearly insufficient to produce mixing but the shorter-period internal waves are potentially able to mix important portions of the water column in the vicinity of the shelf break, where internal waves are likely generated. This is suggested by the mixing efficiency ratio computed using the total energy available in the wave field in this area (station E1), and further confirmed by (i) the fact that internal energy away from the continental shelf drops abruptly (station E2), indicating that the existing energy near the shelf break has been dissipated, and (ii) the analysis of the gradient Richardson number, R_i , which reaches critical values near the canyon's head (station E1).

The analysis of mixing based on the behaviour of R_i has been extended to the region outside (but close to) the Portimao canyon and it suggests that mixing is a quite probable process throughout the area. Moreover, the patches where R_i is critical depict a straight-line-like pattern, which strongly recalls the path of internal beams. This fact points at the internal wave as the driving mechanism for the rather generalised mixing in the area.

Acknowledgments

The authors thank Project MAR99-0643, funded by the Spanish government, for making possible the acquisition of the observations used in the present manuscript. We thank, as well, the Spanish Navy Hydrographic Institute for supplying the research vessels that complemented our initial field experiments.

References

Bruno, M., Mañanes, R., Alonso, J.J., Izquierdo, A., Tejedor, L., Kagan, B., 2000. Vertical structure of the semidiurnal tidal currents at Camarinal Sill, the strait of Gibraltar. *Oceanologica Acta* 23 (1), 15–24.

- Bruno, M., Alonso, J.J., Cózar, A., Vidal, J., Echevarría, F., Ruiz, J., Ruiz-Cañavate, A., Gómez, F., 2002. The boiling water phenomena at Camarinal sill, the Strait of Gibraltar. *Deep-Sea Research II* 49, 4097–4113.
- Candela, J., Winant, C.D., Ruiz, A., 1990. Tides in the Strait of Gibraltar. *Journal of Geophysical Research* 95, 7317–7335.
- Folkard, A.M., Davies, P., Fiúza, A., Ambar, I., 1997. Remotely sensed sea surface thermal patterns in the Gulf of Cádiz and the Strait of Gibraltar: variability, correlations and relationships with the surface wind field. *Journal of Geophysical Research* 102 (C3), 5669–5683.
- García Lafuente, J., Sarhan, T., Vargas, M., Vargas, J.M., Plaza, F., 1999. Tidal motions and tidally induced fluxes through La Línea submarine canyon, western Alboran Sea. *Journal of Geophysical Research* 104 (C2), 3109–3119.
- García Lafuente, J., Vargas, J.M., Plaza, F., Sarhan, T., Candela, J., Bascheck, B., 2000. Tide at the eastern section of the Strait of Gibraltar. *Journal of Geophysical Research* 105 (C6), 14197–14213.
- García Lafuente, J., Delgado, J., Criado Aldeanueva, F., Bruno M., Vargas J. M., 2006. Water Masses Circulation in the Continental Shelf of the Gulf of Cádiz. *Deep-Sea Research II*, this issue [doi:10.1016/j.dsr2.2006.04.015].
- Gill, A.E., 1982. In: William, De., Donn, L. (Eds.), *Atmosphere-Ocean Dynamics*, Academic Press, International Geophysics Series, 661pp.
- Goring, D.K., Henry, R.F., 1998. Short period (1–4 h) sea level fluctuations on the Canterbury coast, New Zealand. *New Zealand Journal of Marine and Freshwater Research* 32, 119–134.
- Holloway, P.E., 1987. Internal Hydraulic jumps and solitons at a shelf-break region on the Australian North–West Shelf. *Journal of Geophysical Research* 92, 5405–5416.
- Kundu, P.K., 1990. *Fluid Mechanics*. New York, Academic Press, (658pp).
- Kundu, P.K., Allen, J.S., Smith, R.L., 1975. Modal decomposition of the velocity field near the Oregon coast. *Journal of Physical Oceanography* 5, 638–704.
- Mysak, L.A., 1980. Topographically trapped waves. *Annual Review of Fluid Mechanics* 12, 45–76.
- New, A.L., 1988. Internal tidal mixing in the Bay of Biscay. *Deep-Sea Research* 35 (5), 691–709.
- Osborne, T.R., 1980. Estimates of the local rate of vertical diffusion from dissipation measurements. *Journal of Physical Oceanography* 10, 83–89.
- Peltier, W.R., Caulfield, C.P., 2003. Mixing efficiency in stratified shear flows. *Annual Review Fluid Mechanics* 35, 135–167.
- Petruncio, E.T., Rosenfeld, L.K., Paduan, J.D., 1998. Observations of the internal tide in Monterey Canyon. *Journal of Physical Oceanography* 28, 1873–1903.
- Sandstrom, H., 1966. The importance of topography in generation and propagation of internal waves. Ph.D. Thesis, University of California, San Diego.
- Vlasenko, V., Alpers, W., 2005. Generation of secondary internal waves by the interaction of an internal solitary wave with an underwater bank. *Journal of Geophysical Research* 110, C02019.
- Wunsch, C., 1968. On the propagation of internal waves up a slope. *Deep-Sea Research* 15, 251–258.